Periodically sheared 2D Yukawa systems

Anikó Zsuzsa Kovács,[1] Peter Hartmann,[1,2] and Zoltán Donkó[1,3]
[1]Institute for Solid State Physics and Optics, Wigner Research Centre for Physics, Hungarian Academy of Sciences, Konkoly-Thege Miklós str. 29-33, H-1121 Budapest, Hungary
[2]Center for Astrophysics, Space Physics and Engineering Research (CASPER), One Bear Place 97310, Baylor University, Waco, Texas 76798, USA
[3]Physics Department, Boston College, Chestnut Hill, Massachusetts 20467, USA

(Received 14 July 2015; accepted 1 October 2015; published online 15 October 2015)

We present non-equilibrium molecular dynamics simulation studies on the dynamic (complex) shear viscosity of a 2D Yukawa system. We have identified a non-monotonic frequency dependence of the viscosity at high frequencies and shear rates, an energy absorption maximum (local resonance) at the Einstein frequency of the system at medium shear rates, an enhanced collective wave activity, when the excitation is near the plateau frequency of the longitudinal wave dispersion, and the emergence of significant configurational anisotropy at small frequencies and high shear rates. © *2015 AIP Publishing LLC*. [http://dx.doi.org/10.1063/1.4933132]

I. INTRODUCTION

The Debye-Hückel (or Yukawa) model has been widely and successfully used to describe the interaction of dust particles in single layered laboratory dusty plasma systems (see, e.g., Ref. 1) and electrically charged colloidal suspensions.[2] In this model, the inter-particle interaction potential energy is given by

$$\Phi(r) = \frac{Q^2}{4\pi\varepsilon_0}\frac{\exp[-r/\lambda_D]}{r}, \quad (1)$$

where Q is the grain electric charge and λ_D is the Debye screening length. Unbounded equilibrium Yukawa systems can be fully characterized by two dimensionless quantities: the Coulomb coupling parameter $\Gamma = Q^2/(4\pi\varepsilon_0 a k_B T)$, where T is the temperature, and the Yukawa screening parameter $\kappa = a/\lambda_D$, where $a = 1/\sqrt{\pi n}$ is the 2D Wigner-Seitz radius and n is the dust areal number density.

Viscosity, the measure of the plastic response of matter (primarily liquids and soft matter) to applied forces, is the central quantity in rheology. For a Newtonian fluid a constant shear viscosity η relates the shear stress σ to the shear rate $\dot{\gamma} = \partial v_x/\partial y$ (transverse velocity gradient) as $\sigma = -\eta\dot{\gamma} = -\eta(\partial v_x/\partial y)$. Regarding complex plasmas, the first experiment on a single layer (2D) dust cloud with control over the applied shear, via adjusting the power of a manipulating laser beam, was carried out by the group of Lin I *et al.* in 2001.[3] Similarly, an experiment making use of a single shearing laser beam was reported.[4] In these experiments, a sheared velocity profile was created around the beam. In another experiment two displaced, parallel counter-propagating laser beams were used to realize a planar Couette configuration in a 2D dusty plasma layer.[5] In another experiment, the non-Newtonian behavior of a 3D complex plasma in the liquid state was identified by Ivlev *et al.*,[6] and investigated in 2D in detail by Gavrikov *et al.*[7,8] Motivated by these pioneering studies, more recently, detailed dusty plasma experiments demonstrated the presence of viscoelastic response[9] and revealed the wave-number dependence of the viscosity in 2D.[10] Experiments in the crystalline phase have identified the slipping of individual crystal lines to be the primary mechanism for relaxing an applied shear stress.[11] Experiment at weaker coupling showed the predicted increase of viscosity with increasing temperature.[12] Lately, we have performed dusty plasma experiments confirming the non-Newtonian (shear-thinning) character of the shear viscosity in 2D with stationary shear.[13] These results were independently confirmed.[14] In addition, we have shown experimental results on the complex shear viscosity, the response of the system to an oscillatory shear in 2D dusty plasmas.[13]

Complementing the experimental efforts, the shear viscosity has been derived in a number of simulation studies,[15–19] both for three-dimensional (3D) and two-dimensional (2D) settings. Besides calculations of the "equilibrium" ($\dot{\gamma} \to 0$) static viscosity, predictions for the shear-thinning effect (typical for complex molecular liquids) were given at high shear rates.[20] The frequency dependence of the complex shear viscosity, which combines the viscous and the elastic components of the complex response of matter to oscillating shear stress as $\eta(\omega) = \eta'(\omega) - i\eta''(\omega)$, was computed for 3D Yukawa liquids.[21] Fundamental questions about the existence or nonexistence of well defined transport coefficients in 2D were addressed.[22]

Here, we present systematic studies of the complex viscosity, covering a large parameter regime in both the $\dot{\gamma}$ shear rate and ω_{shear} oscillation frequency of 2D Yukawa systems, with relevance to laboratory dusty plasma experiments. In addition to the real and imaginary components of the complex shear viscosity, we supply detailed analysis of the energy dissipation, wave generation, and structural consequences of the applied oscillatory shear.

The paper is structured as follows. Section II describes the details of the numerical methods. Section III discusses our numerical results. Section IV summarizes the work.

II. NUMERICAL SIMULATION

In this section, we present the methods used in the present study: (a) Non-equilibrium molecular dynamics simulation

(NEMD) and (b) Langevin dynamics simulation (LD). As Yukawa systems are characterized by dimensionless quantities (Γ and κ), also the results of the simulations are presented in dimensionless units, which relate to physical quantities in SI units as:

- Shear frequency: $\bar{\omega} = \omega_{\text{shear}}/\omega_p$, where $\omega_p = Q\sqrt{n/2\varepsilon_0 ma}$ is the 2D nominal plasma frequency,
- Shear rate: $\bar{\dot{\gamma}} = \dot{\gamma}/\dot{\gamma}_0 = (\partial v_x/\partial y)/(a/v_{\text{therm}})$, where $v_{\text{therm}} = \sqrt{2k_B T/m}$ is the thermal velocity,
- Viscosity: $\bar{\eta} = \eta/\eta_0 = \eta/mn\omega_p a^2$.

Some input parameters are taken from experiments[13]

- Yukawa screening parameter $\kappa = 1.2$.
- Wigner-Seitz radius $a = 315 \times 10^{-6}$ m.
- Charge of a particle $Q = -4840\,e$.
- Mass of a particle $m = 6.64 \times 10^{-14}$ kg.

During the simulations, we track the positions and velocities of all the particles and measure the shear stress by computing the off-diagonal elements of the pressure tensor (shear stress) in every time step of the simulation

$$P_{xy} = \sum_{i=1}^{N}\left[mv_{ix}v_{iy} - \frac{1}{2}\sum_{j\neq i}^{N}\frac{x_{ij}y_{ij}}{r_{ij}}\frac{\partial\Phi(r_{ij})}{\partial r_{ij}}\right], \tag{2}$$

where $N = 11\,400$ is the number of particles and $r_{ij} = |\mathbf{r}_i - \mathbf{r}_j| = |(x_{ij}, y_{ij})|$. From these data, we obtain the complex viscosity in three steps:

(1) We calculate the magnitude of the viscosity $|\eta(\omega)|$ as the ratio of the amplitude of $-P_{xy}(t)$ and the amplitude of the applied shear $\bar{\dot{\gamma}}$.
(2) We calculate the phase angle between $-P_{xy}(t)$ and $\dot{\gamma}(t)$. For illustration, time series are shown in Fig. 1, where the black line represents one period of the harmonic excitation ($\dot{\gamma}(t)$), and colored lines show the response of the system ($-P_{xy}(t)$).
(3) We combine the phase angle and the magnitude of $\eta(\omega)$ and obtain the complex value of the shear viscosity.

These steps are performed assuming linear response of the system. The amplitude and the phase shift of the measured shear stress functions are determined by least-square fitting $\propto \cos(\omega_{\text{shear}}t - \Theta)$ type functions. The NEMD and LD simulations differ in the way the homogeneous shear is induced in the system and in the thermostats. In the following, we briefly introduce both methods.

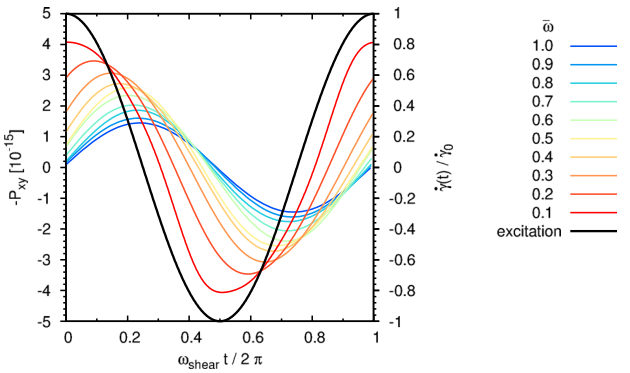

FIG. 1. Off-diagonal element of time-dependent pressure tensor $P_{xy}(t)$ (left scale, colored lines), for a series of perturbation frequencies $\bar{\omega} = \omega_{\text{shear}}/\omega_p$, and the time dependent shear rate $\dot{\gamma}(t)/\dot{\gamma}_0 = \bar{\dot{\gamma}}\cos(\omega_{\text{shear}}t)$ (right scale, black line) for $\bar{\dot{\gamma}} = 1.0$ and $\Gamma = 200$ (liquid phase) at $\kappa = 1.2$. The horizontal axis covers one period of the applied oscillatory shear.

A. Nonequilibrium molecular dynamics simulation

In the NEMD simulation, we use a homogeneous shear algorithm, which generates planar Couette flow.[23] In this algorithm, the shear flow is induced by the movement of the image cells (Lees-Edwards/sliding brick periodic boundary conditions, for illustration see Fig. 2), which is used in conjunction with the Gaussian thermostated SLLOD equations of motion

$$\begin{aligned}\frac{d\mathbf{r}_i}{dt} &= \frac{\tilde{\mathbf{p}}_i}{m} + \dot{\gamma}y_i\hat{\mathbf{x}}\\ \frac{d\tilde{\mathbf{p}}_i}{dt} &= \mathbf{F}_i - \dot{\gamma}\tilde{\mathbf{p}}_{yi}\hat{x} - \alpha\tilde{\mathbf{p}}_i,\end{aligned} \tag{3}$$

where $\tilde{\mathbf{p}}$ is the peculiar momentum of particles, $\dot{\gamma} = \partial v_x/\partial y$ is the shear rate, $\hat{\mathbf{x}}$ is the unit vector in x direction, $\mathbf{F}_i$ is the force acting on particle i due to the pair interactions with the particles in the system, and α is the Gaussian thermostating multiplier, calculated in a way to ensure constant peculiar kinetic energy. The integration of this set of equations is accomplished by the operator-splitting technique.[24] The frequency dependent shear is induced by the harmonic movement of the periodic image cells.

Clearly, this is our preferred method to study viscoelastic phenomena, as it provides a fully homogeneous shear with absolute control of the shear rate. Some preliminary results obtained with this method have already been presented.[25] Nevertheless, this method has its limitations in the regime of low frequencies combined with high shear rates. In these cases, especially in the solid phase, we observe phase separation. This happens due to the interplay of increased ordering due to the alignment of particles into lanes (layers) caused by the large and rapid displacements of neighboring particle rows, and the *global* nature of the Gaussian thermostat. The Gaussian thermostat ensures a constant average (peculiar, thermal) kinetic energy of the particles. This is usually realized by a homogeneous and uni-modal velocity distribution

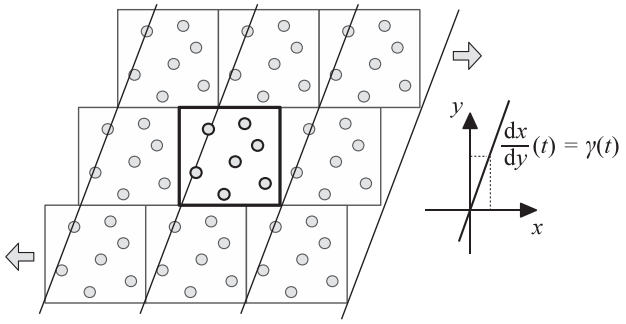

FIG. 2. Illustration of the Lees-Edwards/sliding brick periodic boundary conditions. The principle simulation box (center) is sheared, while its periodic image cells are sheared and displaced simultaneously to provide homogeneous shear.

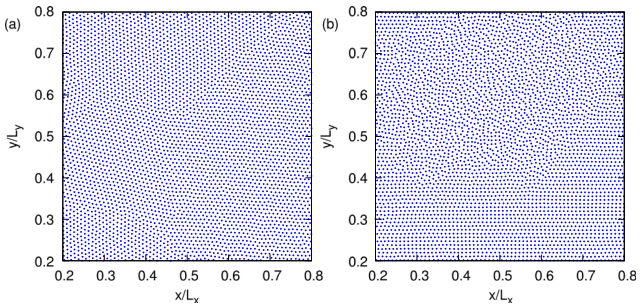

FIG. 3. Particle snapshots from NEMD simulations with $\Gamma = 500$ and (a) $\bar{\omega} = 0.8$, $\bar{\gamma} = 0.04$ [high frequency, low shear rate], and (b) $\bar{\omega} = 0.1$, $\bar{\gamma} = 2.56$ [low frequency, high shear rate].

(e.g., Maxwellian in thermal equilibrium). In the case of low frequency, large amplitude, we observe the segregation of the system into a highly ordered and a disordered part, realizing a bi-modal kinetic energy distribution, with the desired average.

Figure 3 shows two particle snapshots from two cases representing opposing corners of the parameter regime of interest. For high frequency and low shear rate, the displacements of neighboring particles are small, and the snapshot in Fig. 3(a) shows a usual, polycrystalline structure with almost no sign of horizontal (x directional) ordering. In contrast, at low frequency and high shear rate, the above described horizontal ordering and phase separation appears in Fig. 3(b). This effect is clearly unwanted and unphysical, which lets us conclude that the Gaussian thermostated SLLOD fails in this limit. To be able to cover the full parameter regime of interest, we have implemented a Langevin dynamics simulation, where the interplay between friction and stochastic fluctuations realizes a *local* temperature control, which acts on each individual particle separately, not only adjusting the average thermal kinetic energy.

B. Langevin dynamics simulation

In the Langevin simulation, we induce the shear by an external shearing force, which is added to the Langevin equations of motion. The Langevin thermostat ensures a stationary kinetic energy with small fluctuations. The equation of motion for the ith particle is

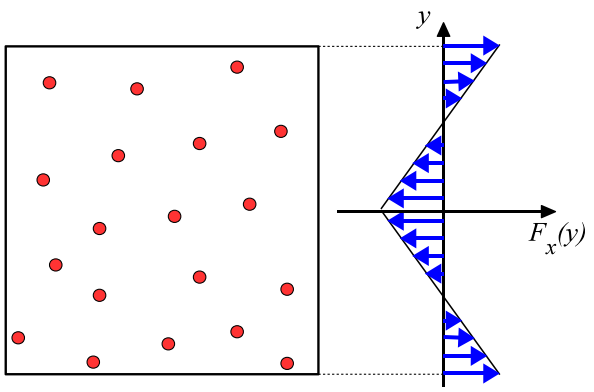

FIG. 4. Illustration of the external shearing force field applied in the Langevin Dynamics simulations. The force field follows the periodicity of the boundary conditions and results in a zero net drift of the systems.

$$\begin{aligned} \frac{d\mathbf{r}_i}{dt} &= \frac{\mathbf{p}_i}{m} \\ \frac{d\mathbf{p}_i}{dt} &= \sum_j \mathbf{F}_{ij} + \mathbf{F}_{i,\mathrm{ext}} - \nu m \mathbf{v} + \mathbf{R}_i, \end{aligned} \tag{4}$$

where $\mathbf{p}_i$ is the momentum of particle i, $\sum_j \mathbf{F}_{ij}$ is the sum of the inter-particle forces acting on particle i, while $\mathbf{F}_{i,\mathrm{ext}}$ represents the external forces, ν is the friction coefficient, and $\mathbf{R}_i$ is a stochastic (random) force. The random force, together with the friction term represents the thermal excitation and damping originating from the gas discharge plasma background in dusty plasma experiments. The friction coefficient was chosen to be $\nu/\omega_p = 0.05$ to closely match our earlier experimental conditions already referred to Ref. 13.

The $\mathbf{F}_{i,\mathrm{ext}}$ external force acts in x direction with magnitude (in parts) linearly dependent on the particles' y coordinate. For illustration, see Fig. 4. The shear rate can only be set indirectly, through scaling the magnitude of the shearing force field. The developing shear is not homogeneous, but it is found to be fairly constant in the domains $0.1 < y/L_y < 0.4$ and $0.6 < y/L_y < 0.9$. The response of the particles in these lower and upper regimes is measured individually and is averaged.

The results of the two methods completely overlap, except for the solid phase in the low frequency, high shear rate corner of the parameter space, where the Gaussian thermostated SLLOD fails. In this regime, the Langevin dynamics simulation results are shown.

III. NUMERICAL RESULTS

In the small shear limit, our simulation results are in qualitative agreement with 3D simulation results.[21] Compared to our previous dusty plasma experiment,[13] we obtain good quantitative agreement for the complex viscosity: (i) the shear rate dependence of the viscosity at static shear shows the same amount of shear thinning, and (ii) increasing the perturbation frequency, the elastic contribution becomes dominant over the dissipative one. This comparison serves as an experimental verification of our simulations and supports its validity in parameter regimes not yet explored experimentally.

During the investigation of the response to harmonic shear, first we focus on the complex shear viscosity and its real–imaginary decomposition. In Fig. 5(a), which represents a relatively low shear rate situation ($\bar{\gamma} = 0.04$) of a liquid, one can observe the total viscosity monotonically decaying with increasing frequency. This characteristic is a superposition of the viscous ($\eta' = \mathrm{Re}[\eta]$) and elastic ($-\eta'' = \mathrm{Im}[\eta]$) contributions, which show a characteristic cross-over frequency, related to the Maxwell relaxation time of the system.[26] In contrast, at high shear rates, as shown in Fig. 5(b) for $\bar{\gamma} = 4$, the magnitude of the viscosity is reduced by about one order of magnitude compared to that at $\bar{\gamma} = 0.04$ (shear thinning), the slope becomes non-monotonic, and the a cross-over frequency of the two contributions is shifted to higher values.

The color maps in Fig. 6, constructed from 100 independent simulations, show the magnitude, complex

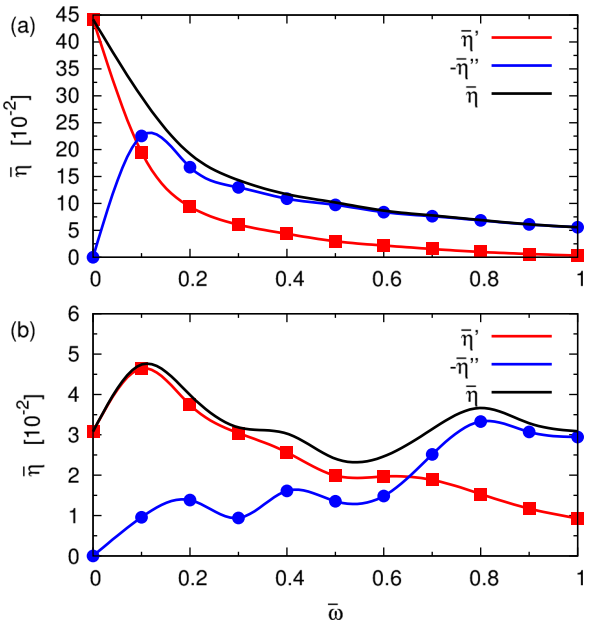

FIG. 5. Magnitude (η), viscous ($\eta' = \mathrm{Re}[\eta]$), and elastic ($-\eta'' = \mathrm{Im}[\eta]$) components of the complex viscosity as a function of $\bar{\omega}$ perturbation frequencies. The shear rates are: (a) $\bar{\gamma} = 0.04$ and (b) $\bar{\gamma} = 4$. The systems are in the liquid phase with $\Gamma = 200$.

argument, and real and imaginary components of the complex viscosity in the full parameter space covered in this work, which are: $0.04 \leq \bar{\gamma} \leq 4$ and $0.1 \leq \bar{\omega} \leq 1$. As a reminder, the complex argument is the phase shift of the pressure oscillation (response) and the oscillation of the applied shear (excitation), as shown in Fig. 1. Monotonic shear thinning can be observed for every frequency value as functions of the shear rate. The frequency dependence at fixed shear rates, however, changes from monotonic to non-monotonic at around $\bar{\gamma} \approx 1$. The decomposition into η' viscous and η'' elastic contributions reveals that the observed non-monotonicity of the magnitude results from the emerging dominance of the elastic response at high shear rates and frequencies.

To gain more insight into the microscopic processes dominating the complex response, we have measured the amount of energy absorbed by the Gaussian thermostat acting on the system. Fig. 7(a) shows that the most efficient heating occurs roughly along a diagonal in the parameter space. This can be qualitatively understood as: (i) At small shear rates and high frequencies, the displacement (in x) of neighboring particles (in y) is small, and the local particle environments do not change during one rapid cycle. The energy of the deformation is stored elastically and does not dissipate into particle mixing. (ii) At high shear rates and low frequencies, the particle displacements are large, and lane formation sets in resulting in easy sliding of the horizontally quasi-ordered particle configuration. The deformation requires relatively low energy. (iii) Around the diagonal of the parameter space, the uncorrelated thermal motion prevents lane formation on one hand, and the displacements on the other hand are already large enough to cause significant changes in the local particle environment, driving particle mixing resulting in a strong energy dissipation. Superimposed to this general structure one can observe that at

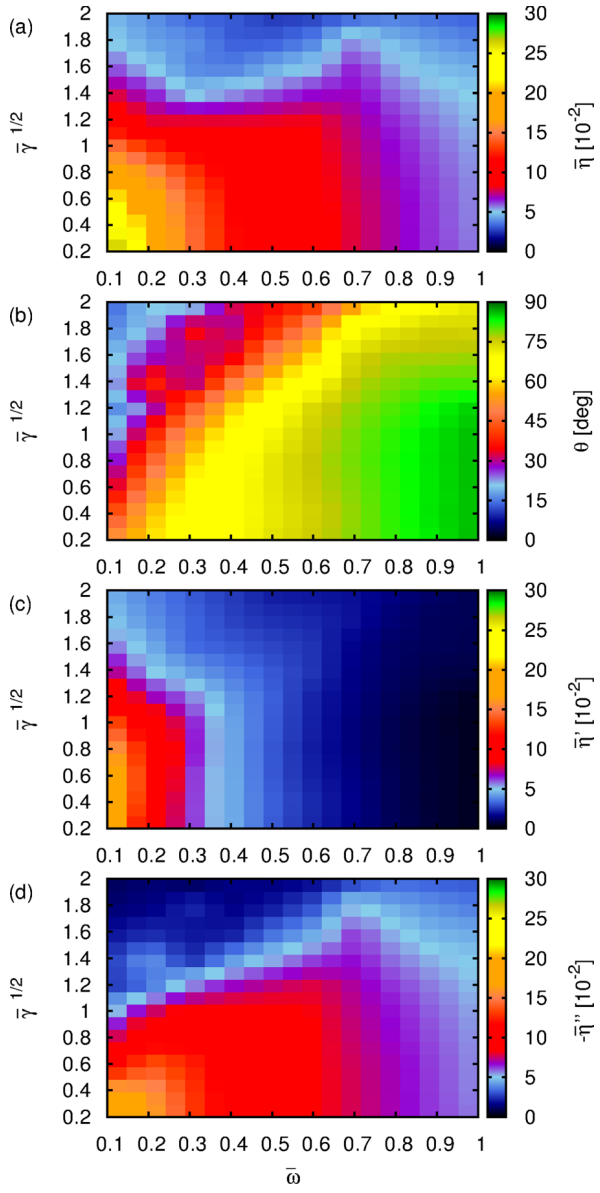

FIG. 6. Magnitude (a), complex argument (b), and real (c) and imaginary (d) parts of the shear viscosity $\eta(\bar{\omega}, \bar{\gamma})$ for $\Gamma = 200$.

$\bar{\omega} \approx 0.4$ a local maximum (resonance) develops in the systems at intermediate shear rates, while around $\bar{\omega} \approx 0.6 - 0.7$ and higher shear rates the system absorbs relatively small amount of heat from the external excitation.

A possible explanation for the resonance is that a 2D Yukawa system with $\kappa = 1.2$ in the strongly coupled liquid phase has a characteristic Einstein frequency[27] of about $\omega_E/\omega_p \approx 0.45$.[28] The Einstein frequency is the frequency of oscillation of a single particle around its equilibrium position in the immobilized frozen environment of the other particles in the system. These single particle oscillations are uncorrelated in space and time. If these oscillations are externally excited, e.g., by external periodic deformations, the energy input from the excitation is efficiently converted into thermal motion.

The local minimum in the absorbed energy seems to coincide with the $\omega/\omega_p \approx 0.62$ peak frequency of the $g_L(\omega)$

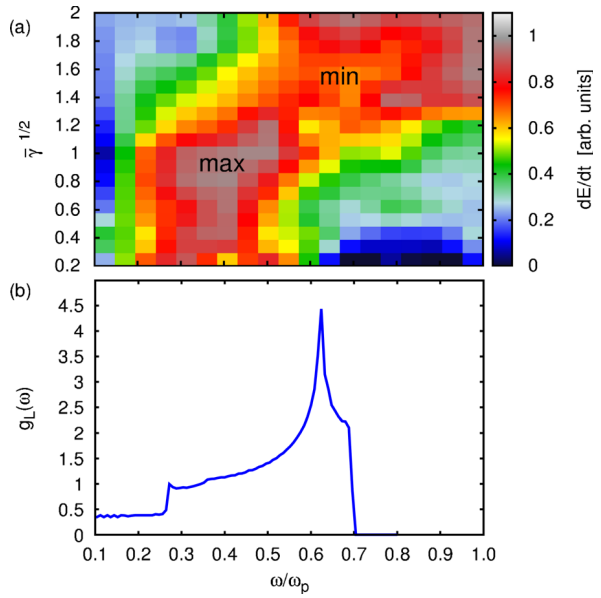

FIG. 7. (a) Energy absorbed by the thermostat (in arb. units) for a series of $\bar{\omega}$ perturbation frequencies and $\bar{\gamma}$ shear rates at $\Gamma = 200$ (liquid). Labels *max* and *min* indicate the positions of the local absorption maximum and minimum. (b) Approximate longitudinal mode wave frequency spectrum of the $\kappa = 1.2$ ground state hexagonal 2D Yukawa lattice.

longitudinal wave frequency spectrum (equivalent to the density of states) of the unperturbed ground state 2D Yukawa lattice. In contrast to Einstein oscillations, these frequencies belong to correlated wave activity, with well defined wavelength (wave number) and amplitude. To obtain the frequency distribution $g_L(\omega)$, we have performed lattice summation on the unperturbed 2D hexagonal (triangular) lattice.[29] First we calculate the $\omega_L(\mathbf{k})$ longitudinal wave dispersion curves of the perfect Yukawa lattice for a set of propagation directions of the wave number vector $\mathbf{k}$ with 1 degree angular resolution. The propagation angle is the angle enclosed between the nearest neighbor bond direction and $\mathbf{k}$. Wave numbers in the range $0 \leq ka \leq 6.6$ with steps of $\Delta ka = 0.05$ were computed. The $g_L(\omega)$ frequency spectrum, as shown in Fig. 7(b), is the normalized histogram ($\int g_L(\omega)\, d\omega = 1$) of all the computed frequency values.

To further support the hypothesis that the local minimum in the energy absorbance is connected to enhanced collective mode excitation relative to the uncorrelated thermal excitation channel, we include the longitudinal current fluctuation spectra calculation in the NEMD simulations.[28] The longitudinal current fluctuation spectrum $L(k,\omega)$ relates to the well known dynamical structure function as $L(k,\omega) = \omega^2 S(k,\omega)$, and as shown later in this manuscript, quantifies the spectral power of the waves propagating in the system at given frequency and wavelength (wave-number). Large amplitude and long lifetime oscillations result in large values of $L(k,\omega)$, while weak modes result small values. To measure the overall wave activity in the system under periodic shear excitation, we can compare the maximum (peak) values of the calculated $L(k,\omega)$ functions. Fig. 8 shows the peak intensities of the $L(k,\omega)$ longitudinal current fluctuation spectra. In this case, the simulations are performed in the solid phase ($\Gamma = 500$), and the fluctuation spectra are

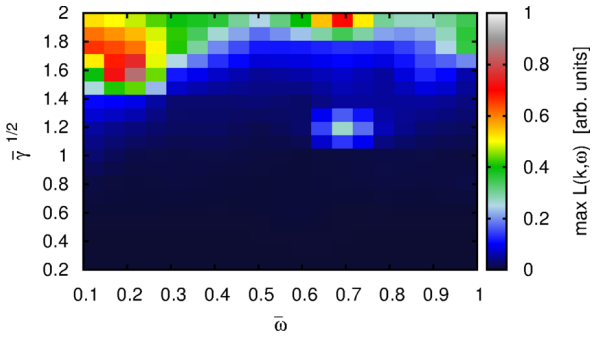

FIG. 8. Longitudinal current fluctuation maximums for a series of $\bar{\omega}$ perturbation frequencies and $\bar{\gamma}$ shear rates at $\Gamma = 500$ (solid phase, for better contrast).

calculated for wave number vectors pointing in the x direction. Although the random initial conditions do not prefer orientation of the resulting solid structure, due to strong shear, however, we observe a tendency of orientation of the nearest neighbor bond along the x axes. Locally enhanced collective wave activity is observed, when the excitation frequency and shear rate are in the vicinity of the observed local absorbance minimum, indicating the long living nature and large amplitude of the excited collective modes (waves) in the system. Usually, one would expect that a resonant type wave excitation finally relaxes to an enhanced heat absorption. As shown above, here we observe a local minimum in the energy absorbance. A clue to the understanding of this counterintuitive observation can be found in Fig. 9, showing two particle snapshots from two different phases of the harmonic excitation of a polycrystalline solid ($\Gamma = 500$). Comparing the configurations at the turnover point of the deformation, where the shear related velocities are zero ($\dot{\gamma}(t) = 0$, Fig. 9(a)) and at the maximum shear rate ($\dot{\gamma}(t)/\gamma_0 = \bar{\gamma}$, Fig. 9(b)), one can clearly identify diagonally aligned compressional type density wave formation in the latter case. It seems that the long lifetime of these collective oscillations, in combination with the relatively high excitation frequency, results in a reversible mechanism. During the first quarter cycle of the harmonic shear excitation, the density waves grow in the system, while during the second quarter, these waves relax returning the elastically stored energy to the excitation instead of being damped and transformed to heat. In the second half of the excitation cycle, this is repeated in the other diagonal direction.

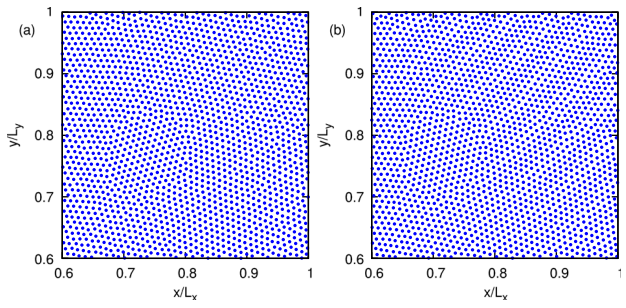

FIG. 9. Particle snapshots during different phases of the periodic shearing excitation: (a) the turnover ($\dot{\gamma}(t) = 0$) point and (b) the maximum velocity phase ($\dot{\gamma}(t) = \max.$) of the applied shear for $\Gamma = 500$, $\bar{\gamma} = 2.56$, and $\bar{\omega} = 0.8$.

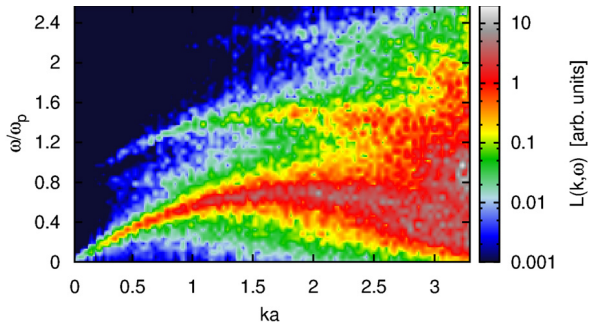

FIG. 10. $L(k,\omega)$ longitudinal current fluctuation spectrum for $\Gamma = 200$, $\bar{\gamma} = 0.04$, and $\bar{\omega} = 0.8$.

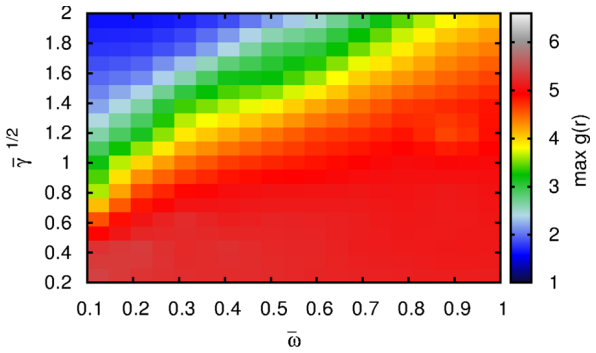

FIG. 12. Amplitude of the first peak of the pair correlation function for a series of $\bar{\omega}$ perturbation frequencies and $\bar{\gamma}$ shear rates at $\Gamma = 500$.

Besides resonant excitation of some collective modes, the shearing excitation affects the overall mode structure of the current fluctuations in the system. Figure 10 shows the longitudinal current fluctuation spectrum of the $\Gamma = 200$ system exposed to small ($\bar{\gamma} = 0.04$), but a relatively high frequency ($\bar{\omega} = 0.8$) oscillatory shear. The principal, acoustic mode, with a dispersion equivalent to that of the unperturbed system, has the highest intensity. In addition, new modes with lower intensity appear as replicas of the principal mode shifted up in frequency exactly by the amount of the applied excitation frequency.

At higher shear rates, the longitudinal current fluctuation spectrum shows qualitatively new features, as it can be seen from Fig. 11. First, a step forms, which divides the parameters space into a nearly fluctuation free regime at low wave numbers and high frequencies and a regime with increased wave activity. The frequency of this borderline has a linear dependence on the wave number. Second, in the active region, horizontal lines appear in the spectrum at frequencies $\omega/\omega_p = (2M+1)\bar{\omega}$, where $M \in \mathbb{Z}$. The intensities of the horizontal modes increase with increasing frequency.

The presence of the background gas in dusty plasma experiments, which was taken into account in our Langevin dynamics studies with the friction term in Eq. (4) can result in damping, or in high pressure experiments even in complete suppression of propagating waves. In our case, due to the low value of the friction coefficient ($\nu/\omega_p = 0.05$), we experience only a slight broadening of spectral lines obtained by Langevin dynamics simulations compared to the frictionless NEMD calculations.

To illustrate changes in the positional structure in the systems due to the applied oscillatory shear, we show in Fig. 12 the amplitude of the first peak of the $g(r)$ pair correlation function (PCF). A complex behavior is observed with a few competing trends. At lower shear rates, the amplitude of the first peak of the PCF increases with frequency, while at high frequencies, a maximum of the peak magnitude appears as the shear rate increases. As already mentioned earlier, at large shear rates and low frequencies a significant ordering of the

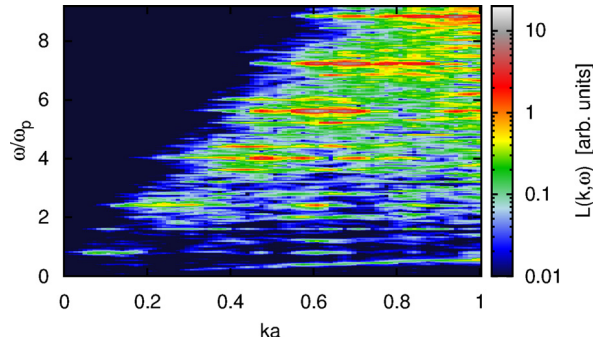

FIG. 11. $L(k,\omega)$ longitudinal current fluctuation spectrum for $\Gamma = 500$, $\bar{\gamma} = 2.56$, and $\bar{\omega} = 0.8$.

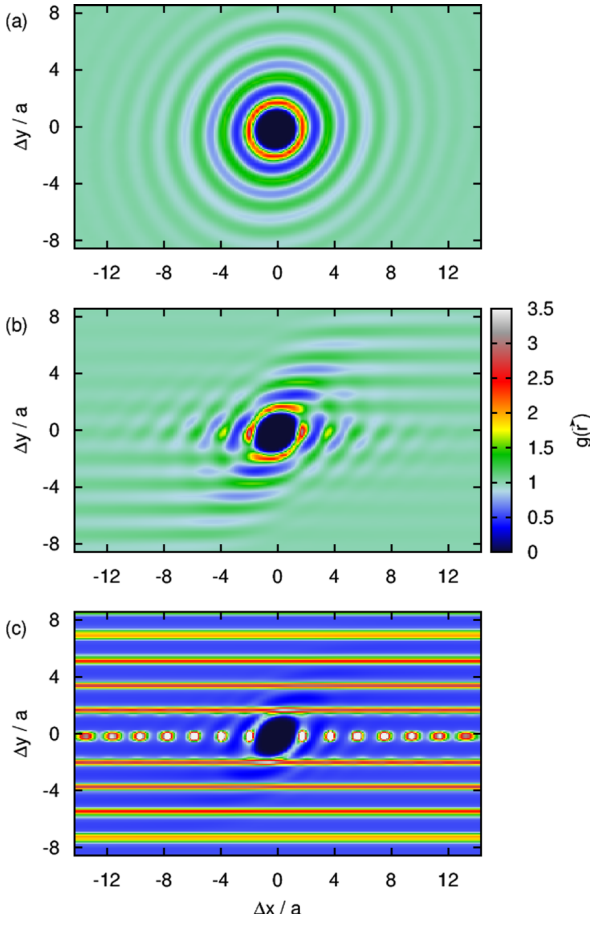

FIG. 13. $g(\vec{r})$ pair correlation function, with $\vec{r} = (\Delta x, \Delta y)$ for systems with $\bar{\omega} = 0$ constant, homogeneous shear rate of (a) $\bar{\gamma} = 0.1$, (b) $\bar{\gamma} = 1$, and (c) $\bar{\gamma} = 2$. Common systems parameters are: $\Gamma = 140$, $\kappa = 1$.

particles into x-directional lanes can be observed in the particle configurations, as illustrated in Fig. 3.

To quantify the tendency of the system to build up structural anisotropy, we have extended the calculation of the pair correlation function from $g(r)$ to $g(\vec{r})$ and systems with $\bar{\omega} = 0$ steady shear. Figure 13 shows the NEMD results for three shear rates for 2D Yukawa liquid with $\Gamma = 140$ and $\kappa = 1$. For the smallest shear rate of $\bar{\gamma} = 0.1$, the anisotropy is negligible, the ring-like structure of the neighbor distributions, typical for liquids, is well preserved. At medium shear ($\bar{\gamma} = 1$), the structure changes from ring-like to anisotropic with the onset of x-directional lane formation. Dusty plasma experiments, where the shear was induced with two parallel, counter-propagating laser beams have already shown similar effects.[30] At higher shear rate ($\bar{\gamma} = 2$), the system forms well separated lanes with deep, but non-zero correlation voids in between. Similar lane formation has been observed during the penetration of small size dust particles into an ensemble of larger dust,[31] and in bi-disperse colloids.[32] Interestingly, the correlations within a lane are also enhanced, compared to the non-perturbed liquid case, as it can be seen at the center lane in Fig. 13(b).

The apparent contradiction that arises comparing the conclusions, drawn from Figs. 12 and 13 about the behavior of positional correlations with increasing shear rate at low frequencies, can be resolved by taking into account the anisotropy of the system. In Fig. 12, the $g(r)$ isotropic pair correlation function shows indeed a decreasing first peak intensity, which is a consequence of the angular averaging of the increasingly anisotropic particle distributions, as shown in Fig. 13. This averaging results in an artificial broadening of the isotropic correlation peaks, ultimately showing lower peak amplitudes.

IV. SUMMARY

By means of first principle numerical simulations of harmonically sheared 2D Yukawa systems, we have identified and partially quantified the following features:

- A non-monotonicity in the frequency dependence of the complex shear viscosity appears due to the competition of viscous and elastic deformations.
- Single particle excitations are responsible for resonant heating at moderate frequencies and shear rates.
- Enhanced collective wave activity is observed when the excitation frequency matches the peak in the frequency distribution function.
- Distinct, high frequency longitudinal current fluctuations modes develop with an odd parity selection rule.
- Structural anisotropy builds up with increasing shear rate realizing lane formation and enhanced correlations in principal directions.

ACKNOWLEDGMENTS

This work has been supported by the OTKA NN-103150 and K-105476 Grants and the János Bolyai Research Scholarship of the Hungarian Academy of Sciences.

[1]G. E. Morfill and A. V. Ivlev, Rev. Mod. Phys. **81**, 1353 (2009); M. Bonitz, C. Henning, and D. Block, Rep. Prog. Phys. **73**, 066501 (2010).
[2]H. Löwen, E. Allahyarov, C. N. Likos, R. Blaak, J. Dzubiella, A. Jusufi, N. Hoffmann, and H. M. Harreis, J. Phys. A: Math. Gen. **36**, 5827 (2003).
[3]W.-T. Juan, M.-H. Chen, and L. I, Phys. Rev. E **64**, 016402 (2001).
[4]A. Gavrikov, I. Shakhova, A. Ivanov, O. Petrov, N. Vorona, and V. Fortov, Phys. Lett. A **336**, 378 (2005).
[5]V. Nosenko and J. Goree, Phys. Rev. Lett. **93**, 155004 (2004).
[6]A. V. Ivlev, V. Steinberg, R. Kompaneets, H. Höfner, I. Sidorenko, and G. E. Morfill, Phys. Rev. Lett. **98**, 145003 (2007).
[7]A. V. Gavrikov, D. N. Goranskaya, A. S. Ivanov, O. F. Petrov, R. A. Timirkhanov, N. A. Vorona, and V. E. Fortov, J. Plasma Phys. **76**, 579 (2010).
[8]N. Vorona, A. Gavrikov, A. Ivanov, O. Petrov, V. Fortov, and I. Shakhova, J. Exp. Theor. Phys. **105**, 824 (2007).
[9]C.-L. Chan and L. I, Phys. Rev. Lett. **98**, 105002 (2007).
[10]Y. Feng, J. Goree, and B. Liu, Phys. Rev. Lett. **105**, 025002 (2010).
[11]C. Durniak and D. Samsonov, Phys. Rev. Lett. **106**, 175001 (2011).
[12]V. E. Fortov, O. F. Petrov, O. S. Vaulina, and R. A. Timirkhanov, Phys. Rev. Lett. **109**, 055002 (2012).
[13]P. Hartmann, M. C. Sándor, A. Kovács, and Z. Donkó, Phys. Rev. E **84**, 016404 (2011).
[14]V. Nosenko, A. V. Ivlev, and G. E. Morfill, Phys. Rev. E **87**, 043115 (2013).
[15]T. Saigo and S. Hamaguchi, Phys. Plasmas **9**, 1210 (2002).
[16]G. Salin and J.-M. Caillol, Phys. Rev. Lett. **88**, 065002 (2002); Phys. Plasmas **10**, 1220 (2003).
[17]K. Y. Sanbonmatsu and M. S. Murillo, Phys. Rev. Lett. **86**, 1215 (2001).
[18]Z. Donkó and P. Hartmann, Phys. Rev. E **78**, 026408 (2008).
[19]T. S. Ramazanov and K. N. Dzhumagulova, Contrib. Plasma Phys. **48**, 357 (2008).
[20]Z. Donkó, J. Goree, P. Hartmann, and K. Kutasi, Phys. Rev. Lett. **96**, 145003 (2006); Z. Donkó, P. Hartmann, and J. Goree, Mod. Phys. Lett. B **21**, 1357 (2007).
[21]Z. Donkó, J. Goree, and P. Hartmann, Phys. Rev. E **81**, 056404 (2010).
[22]Z. Donkó, J. Goree, P. Hartmann, and B. Liu, Phys. Rev. E **79**, 026401 (2009).
[23]D. J. Evans and G. P. Morriss, *Statistical Mechanics of Nonequilibrium Liquids* (Academic Press, New York, 1990).
[24]G. Pan, J. F. Ely, C. McCabe, and D. J. Isbister, J. Chem. Phys. **122**, 094114 (2005).
[25]A. Z. Kovács, P. Hartmann, and Z. Donkó, Contrib. Plasma Phys. **52**, 199 (2012).
[26]J. Goree, Z. Donkó, and P. Hartmann, Phys. Rev. E **85**, 066401 (2012).
[27]A. Einstein, Ann. Phys. **22**, 180 (1907).
[28]Z. Donkó, G. J. Kalman, and P. Hartmann, J. Phys.: Condens. Matter **20**, 413101 (2008).
[29]T. Sullivan, G. J. Kalman, S. Kyrkos, P. Bakshi, M. Rosenberg, and Z. Donko, J. Phys. A: Math. Gen. **39**, 4607 (2006).
[30]V. Nosenko, A. V. Ivlev, and G. E. Morfill, Phys. Rev. Lett. **108**, 135005 (2012).
[31]K. R. Sütterlin, A. Wysocki, A. V. Ivlev, C. Räth, H. M. Thomas, M. Rubin-Zuzic, W. J. Goedheer, V. E. Fortov, A. M. Lipaev, V. I. Molotkov, O. F. Petrov, G. E. Morfill, and H. Löwen, Phys. Rev. Lett. **102**, 085003 (2009).
[32]C. Reichhardt and C. J. O. Reichhardt, Phys. Rev. E **75**, 040402 (2007).